Available *online* at: http://ajeeet.ft.unand.ac.id/
Andalas Journal of Electrical and Electronic Engineering Technology
ISSN 2777-0079

Nonlinear Parameter Identification of the Franka Emika PANDA Robot: A Comparative Analysis of Friction Models

Soto K. Gilbert[1,2], *Francis I. Maina*[2], *Jean B. Byiringiro*[3]

[1] *Smart Mini Factory, The Free University of Bolzano, Bolzano, 39100, Italy*
[2] *Mechatronics Engineering Department, Dedan Kimathi University of Technology, Nyeri, 10100, Kenya*
[3] *Siemens Training and Research Centre, Dedan Kimathi University of Technology, Nyeri, 10100, Kenya*

ARTICLE INFORMATION

Received: April 27, 2024
Revised: July 25, 2024
Accepted: September 16, 2024
Available online: November 30, 2024

KEYWORDS

Parameter Identification, Nonlinear Friction, Lugre, Stribeck, and Sigmoidal Friction Models

CORRESPONDENCE

Phone: +254722119222
E-mail: gsoto@unibz.it

ABSTRACT

This research addresses the problem of dynamic parameter identification for robot manipulators. As the complex manipulation of tasks increases, traditional control methods become insufficient, necessitating accurate model-based control. Previous studies have explored various parameter identification methods for robot manipulators. Still, the impact of different friction models on dynamic parameter identification, particularly for the Franka Emika PANDA robot, is yet to be comprehensively investigated. The linear and nonlinear parameter identification methods and nonlinear friction models (Lugre, Stribeck, and Sigmoidal) were studied on the PANDA robot. A linear inverse dynamic model was developed using the Newton-Euler method. Identification and validation trajectories were designed. Nonlinear constraints and bounds were applied for easier convergence, ensuring a positive definite inertia tensor in the center of mass (COM) frame. Using constrained least squares with Lasso regularisation, model-estimated torques comparison to measurements was done to estimate the physical parameters, considering the PANDA robot's hand as a payload. We obtained the PANDA robot's physical parameters, including the hand's mass, without a friction model where discrepancies in joint torques were observed. Incorporating friction models reduced these discrepancies, validated by another trajectory comparison between the measured and the model's predicted joint torques. Stribeck friction model exhibited the best performance in estimating parameters from its Root Mean Square Error (RMSE) and Mean Absolute Error (MAE), indicating its effectiveness in capturing nonlinearities in the PANDA robot.

INTRODUCTION

Modeling and simulation are critical in robotics as they offer insights into existing systems and enable engineers to develop and test new control algorithms [1],[2]. Accurate control of advanced manipulators requires model-based control techniques, such as computed torque and model predictive control (MPC) [3]–[6], which rely on a precise mathematical model encompassing the manipulator's dynamic parameters. Applications such as collaborative robots require accurate controllers based on dynamic models of the system, as closed-loop control alone may not be feasible or sufficiently accurate in these scenarios [7]–[11].

With advanced manufacturing and automation, industrial manipulators have become increasingly necessary for higher productivity and flexibility in automated production lines, playing a significant role in realizing just-in-time production in modern manufacturing systems [12]–[14]. However, unlike humans with numerous sensory nerves, which are used to perceive changes in their environment and transmit them as electrical signals to the brain, modern robots are limited in sensory and actuation capabilities [15]–[17]. Industrial robots rely on the design of controllers to receive sensor inputs and output the required controls [18]–[20].

Previous studies have explored various parameter identification methods for robot manipulators [21]–[23]. However, the impact of distinct friction models on dynamic parameter identification, particularly for the Franka Emika PANDA robot, has yet to be comprehensively investigated. This study addresses this gap by examining the effects of Lugre, Stribeck, and Sigmoidal nonlinear friction models on the accuracy of retrieved (through nonlinear optimization) parameters.

The primary objective is to accurately identify the physical parameters of the PANDA robot, Figure 1, and investigate the influence of different friction models on the identification process. Specific goals include deriving a symbolic dynamic model for the PANDA robot, designing experiments through nonlinear optimization to obtain exciting trajectories, data acquisition, and signal conditioning from the experiment for analysis, and validating the developed model [7], [24]. Friction

https://doi.org/10.25077/ajeeet.v4i2.101

models are incorporated in the parameter identification process to improve the accuracy of retrieved parameters for the PANDA robot [25], [26]. The most suitable friction model for capturing nonlinearities in the PANDA robot's dynamics is identified by comparing the results obtained using different friction models [27], [28].

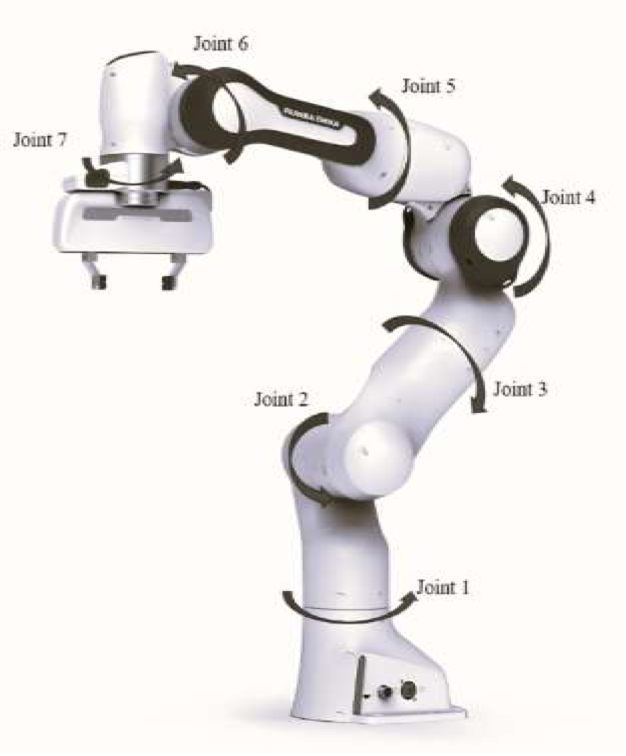

Figure 1: Franka Emika PANDA Robot with all the joints [42]

The research involves the development of a linear inverse dynamic model using the Newton-Euler method [29], [30] and the design of identification and validation trajectories [21], [31]. It also compares model-estimated torques to measurements to estimate physical parameters, considering the PANDA robot's hand as a payload. A validation trajectory will be run to compare measured and predicted joint torques and assess the performance of different friction models [32], [33].

The results of this research will contribute to robotics by providing insights into the effects of different friction models on dynamic parameter identification for robot manipulators, particularly the PANDA robot, which plays a significant role in robot-based research experiments, and a better model could improve the accuracy. Getting precise joint parameters could improve controller design and more accurate control.

The outline of this paper is as follows: Section *METHOD* provides a detailed description of the methodology employed, including developing the inverse dynamic, friction models, identification trajectory, and the parameter identification process. Section ***Error! Reference source not found.*** presents the results and validation of the physical parameters. Finally, section *CONCLUSION* concludes the paper.

METHOD

Identification Models

This section describes the methodology for developing the geometric, kinematic, and dynamic models for the PANDA robot. A modified geometric model is presented, and the modified Denavit-Hartenberg model (Khalil-Kleinfinger) is transformed into a dynamic one.

Geometric Model - modified Denavit-Hartenberg (DH) model (Khalil-Kleinfinger)

To create a linear identification model, the equations of motion need to be linearly expressed in the inertial parameters. Most research on parameter identification uses a modified DH model, specifically the Khalil-Kleinfinger notation, to describe the connection of the links [26]. Therefore, this paper also employs the modified DH model to develop the linear identification model.

The modified DH convention assumes that the i^{th} coordinate frame is at the i^{th} joint [34]. The four parameters describing the orientation of the i^{th} link relative to the i^{th-1} link are presented in Table 1.

Kinematic Model

The transformation matrix was formed from the four elementary transformations represented as can be seen at equation (1):

$$A_i^{i-1} = \begin{bmatrix} C\theta_i & -S\theta_i & 0 & a_{i-1} \\ S\theta_i C\alpha_{i-1} & C\theta_i C\alpha_{i-1} & -S\alpha_{i-1} & -d_i S\alpha_{i-1} \\ S\theta_i S\alpha_{i-1} & C\theta_i S\alpha_{i-1} & C\alpha_{i-1} & d_i C\alpha_{i-1} \\ 0 & 0 & 0 & 1 \end{bmatrix} \quad (1)$$

where $S(\cdot) = \sin(\cdot)$ and $C(\cdot) = \cos(\cdot)$

With the above intermediate transformation matrices taking the form in equation (2):

$$^{i-1}A_i = \begin{bmatrix} ^{i}R_{i-1} & ^{i}O_{i-1} \\ 0 & 1 \end{bmatrix} \quad (2)$$

The end effector's position and orientation were defined in equation (3):

$$H = {}^{0}A_i = {}^{0}A_1 \, {}^{1}A_2 \, {}^{2}A_3 \dots . {}^{i-1} A_i \quad (3)$$

Table 1: DH Parameters for the Franka Emika PANDA robot

Joint (i)	Twist Angle (α_i)	Link Offset (d_i)	Link Length (r_i)	Joint Angle (θ_i)
1	0	0	0.333	$\theta 1$
2	$-\pi/2$	0	0	$\theta 2$
3	$\pi/2$	0	0.316	$\theta 3$
4	$\pi/2$	0.0825	0	$\theta 4$
5	$-\pi/2$	-0.0825	0.384	$\theta 5$
6	$\pi/2$	0	0	$\theta 6$
7	$\pi/2$	0.088	0	$\theta 7$

Table 1 shows the modified DH parameters for the PANDA robot in Khalil-Kleinfinger notation.

Dynamic Model

The forward and inverse dynamic models were created using the Newton-Euler formulation and implemented on the openSYMORO software [35]. The inverse dynamics model was computed using forward and backward recursion techniques [36]. The inertias were represented in their corresponding link frames rather than their center of mass frames using Steiner's law to linearize the Newton-Euler equations.

Inverse Dynamics

The dynamics of a manipulator were described by equation (4):

$$\tau = \mathbf{f}(\theta, \dot{\theta}, \ddot{\theta}) \tag{4}$$

where τ represents the generated joint torques necessary for motion and is calculated using $\mathbf{f}(\theta, \dot{\theta}, \ddot{\theta})$ which is the manipulator's nonlinear function of motion. $\theta, \dot{\theta}$, and $\ddot{\theta}$ represent the position, velocity, and acceleration of the corresponding joints. Equation (4) serves as the basis for both dynamic analysis of the robot and any applicable model-based control techniques and makes no allowance for external forces [37]. The recursive Newton-Euler inverse dynamics method derives the joint torques τ from $\theta, \dot{\theta}, \ddot{\theta}$ as can be seen in equation (5).

$$\tau = M(\theta)\ddot{\theta} + c(\theta, \dot{\theta})\dot{\theta} + g(\theta) \tag{5}$$

If the equations of motion are linearly expressed in inertial parameters [38], the system may be written in the equation (6):

$$\tau = \mathbf{w}(\theta, \dot{\theta}, \ddot{\theta})\mathbf{X} \tag{6}$$

where $\mathbf{X}$ is a vector with n parameter values for each link. The inertial parameters in $\mathbf{X}$ for each link are the mass, inertia tensors in the link frame, and the first moment.

Forward Dynamics

The forward dynamics solve for $\ddot{\theta}$ given τ, θ, and $\dot{\theta}$ in the equation (7):

$$\tau = M(\theta)\ddot{\theta} + c(\theta, \dot{\theta})\dot{\theta} + g(\theta) \tag{7}$$

The inverse dynamics technique was used to solve the forward dynamics by first determining the joint forces and torques when $\ddot{\theta}$, joint accelerations were set to zero. The result was the sum of Coriolis and gravity torques in equation (8):

$$\tau_{\ddot{\theta}=0} = c(\theta, \dot{\theta})\dot{\theta} + g(\theta) \tag{8}$$

The mass matrix $M(\theta)$ was solved by repeatedly invoking inverse dynamics seven times using equation (9).

$$M(\theta) = [M_1(\theta) \quad \cdots \quad M_7(\theta)] \tag{9}$$

where $\tau = M_i(\theta)$ when $\ddot{\theta}_i = 1, \ddot{\theta}_j = 0, \forall j \neq i, \dot{\theta} = 0, g = 0$. With known values of τ, solution (equation 10) was realized:

$$\begin{aligned} M(\theta)\ddot{\theta} &= \tau - c(\theta, \dot{\theta})\dot{\theta} - g(\theta) \\ &= \tau - \tau_{\ddot{\theta}=0} \end{aligned} \tag{10}$$

Equation 10 was used to solve for $\ddot{\theta}$ using Runge-Kutta 4 (RK4). The $\ddot{\theta}$ from the forward dynamics was numerically integrated at each time step. Then, the joint accelerations, $\ddot{\theta}$, the current joint positions, θ, and velocities, $\dot{\theta}$, were used to calculate the positions and velocities at the next time step for simulation purposes.

Friction Models

The measured torques consist of actuator torques (motor), gravity torques, and friction torques. Incorporating a friction model in the robot's inverse dynamics model is vital to prevent the optimizer from bias due to incomplete modeling, which would become apparent during validation (estimated parameters will not account for the missing friction effects). Assuming the identification torques do not account for friction torques and only consider the sum of actuator and gravity torques, discrepancies arise between measured and estimated torques in equation (11) attributed to unmodeled friction torques.

$$\tau_{\text{measured}} - \tau_{\text{estimated}} = \tau_{\text{friction}} \tag{11}$$

While the simple Coulomb and Viscous friction model $\tau_{f,i} = F_{c,i}\,\text{sign}(\dot{\theta}_i) + F_{v,i}\dot{\theta}_i$ is straightforward to implement, it fails to account for nonlinear friction effects and may lead to discontinuities in regions where joint velocities are zero. This is because Coulomb friction is a discontinuous function of velocity, potentially causing the robot to exhibit chattering. Three more advanced friction models are evaluated to address this limitation: Lugre, Stribeck, and Sigmoidal.

In the **Lugre** model, friction torques $\tau_{f,i}$ are formulated as:

$$\tau_{f,i} = \sigma_{0,i}\,\text{sgn}(\dot{\theta}_i - v_{0,i} z_i) + \sigma_{2,i}\dot{\theta}_i S_i + \sigma_{3,i}\dot{\theta}_i(1 - S_i) \tag{12}$$

where $\tau_{f,i}$ is the friction force, $\sigma_{2,i}$ is the viscous friction force, and $\sigma_{3,i}$ is the Stribeck effect. $v_{0,i}$ is the presiding displacement threshold, z_i is the friction model's internal state variable for joint i, and $\dot{\theta}_i$ is the joint velocity for joint i. S_i is the Stribeck function for joint i, and realized from $S_i = 1 - e^{-\frac{|\dot{\theta}_i - v_{1,i}|}{v_{2,i}}}$.

At each time step, the internal state variable z_i is updated using the equation: $z_i(t) = z_i(t-1) + \Delta t\left(\dot{\theta}_i(t) - \frac{\sigma_{0,i}}{\sigma_{1,i}} z_i(t-1)\right)$, where Δt is the time step.

In the **Stribeck** model, the friction torques, τ_f, is calculated using equation (13):

$$\begin{aligned} \text{Stribeck term} &= F_s \cdot \exp\left(-\frac{|\dot{\theta}|}{v_s} \cdot k_s\right), \\ \tau_f &= \text{sgn}(\dot{\theta}) \cdot (F_c + \text{ Striebeckterm }) + \dot{\theta} \cdot F_v. \end{aligned} \tag{13}$$

where τ_f is the Friction torque, F_c the Coulomb friction coefficient, F_v denotes the viscous friction coefficient, F_s is the stiction friction coefficient, v_s corresponds to the Stribeck velocity, k_s is for adjusting the sensitivity of the stiction effect and $\dot{\theta}$ the joint velocities.

The Stribeck term incorporates F_s, v_s, and k_s to account for the nonlinear friction behavior near $\dot{\theta}_i = 0$.

The sigmoidal friction model was formulated as:

$$\tau_{f,i}(\dot{\theta}_i) = \frac{\psi_{1,i}}{1 + e^{-\psi_{2,i}(\dot{\theta}_i + \psi_{3,i})}} - \frac{\psi_{1,i}}{1 + e^{-\psi_{2,i}\psi_{3,i}}} \qquad (14)$$

where $\tau_{f,i}$ is the friction torque for the i^{th} joint, $\dot{\theta}i$ represent joint velocity. $\psi_{1,\text{I}}, \psi_{2,i}$ and $\psi_{3,i}$ are the three friction parameters for each joint. $\psi_{2,i}$ determines the shape of the sigmoidal curve, which influences the transition from static friction to dynamic friction for the i^{th} point. $\psi_{3,i}$ functions as a horizontal displacement for the sigmoidal curve and determines the joint velocity at which the transition from static to dynamic friction occurs for the i^{th} joint.

Trajectory Parametrization

The experiment was designed in two stages. First, a suitable trajectory parametrization was chosen, and then appropriate trajectory parameters were determined.

For each joint i, the angular position θ_i was expressed as a finite Fourier series with a finite sum of sine and cosine functions represented as:

$$\theta_i(t) = \theta_{0,i} + \sum_{l=1}^{L} \frac{a_{l,i}}{l\omega_f} \sin\left(l\omega_f t\right) - \frac{b_{l,i}}{l\omega_f} \cos\left(l\omega_f t\right) \qquad (15)$$

where $i \in \{1,7\}$, for the seven degrees of freedom of the robot, t is the time, ω_f represents the fundamental pulsation of the finite Fourier series, which is the same for all seven joints. $T_f = \frac{2\pi}{\omega_f}$. Each Fourier series contains $2L + 1$ parameters representing degrees of freedom for trajectory optimization. $a_{l,i}$, and $b_{l,i}$ are the amplitudes of the sine and cosine functions, respectively, and $\theta_{0,i}$ is the position offset of the trajectory.

L is the number of summands, $\omega_f = 0.15\pi$ for both identification and validation trajectories. The coefficients $a_{l,i}, b_{l,i}$ and $\theta_{0,i}$ are subject to joint space limits provided by the robot's manufacturer.

Identification

Ensuring Physically Valid Parameters

The linear identification model can be solved easily due to its linearity in the model's inertial parameters. However, there is no assurance that the identified inertial parameters yield a positive definite mass matrix, which is essential for the system to be physically feasible. Therefore, physical parameters which are nonlinear to the model are used. Inertial parameters are derived from physical parameters by applying Steiner's law to inertia tensor and building first moments. The first moment is a product of a vector from the link frame R_i, pointing to the center of mass and linking masses m_i.

$$\begin{aligned} \mathbf{P}_i &= [c_{x_i} m_i \quad c_{y_i} m_i \quad c_{z_i} m_i]^T \\ \mathbf{J}_i &= \mathbf{I}_{Gi} - m_i\left(\mathbf{c}_i^T \mathbf{c}_i \mathbf{E} - \mathbf{c}_i \mathbf{c}_i^T\right) \end{aligned} \qquad (16)$$

where $\mathbf{I}_{Gi}$ is the inertia tensor at the Centre of Mass (COM) frame, and $\mathbf{J}_i$ is the inertia tensor at the origin of the link i frame, R_i.

Inertial parameters in equation (16) cannot ensure a positive definite mass matrix [39]. Instead, physical parameters for the inertia tensor at the COM frame $\mathbf{I}_{Gi}$, and both mass and center of mass for each link are used. The vector of physical parameters $\chi_i^{(\mathbf{p})}$ is given by equation (17):

$$\chi_i^{(\mathbf{p})} = \left[\chi_i^{(I)} \quad \chi_i^{(c)} \quad \chi_i^{(m)}\right]^T \qquad (17)$$

Where:

$$\begin{aligned} \chi_i^{(I)} &= [I_{xx_i} \quad I_{xy_i} \quad I_{xz_i} \quad I_{yy_i} \quad I_{yz_i} \quad I_{zz_i}] = \mathbf{I}_{Gi} \\ \chi_i^{(c)} &= [c_{x_i} \quad c_{y_i} \quad c_{z_i}] \text{ Center of Mass, COM} \\ \chi_i^{(m)} &= m_i \text{ Mass of link i} \end{aligned} \qquad (18)$$

The friction parameters were not included in equation (18). To use physical parameters on the identification model, the base inertial parameters $\mathbf{X}^{(\mathbf{B}_0)}$ are expressed as a function of physical parameters $\left(\chi^{(\mathbf{p})}\right)$ as: $\mathbf{X}^{(\mathbf{B}_0)}\left(\chi^{(\mathbf{p})}\right)$. The re-written equation 4, $\tau = \mathbf{f}\left(\theta, \dot{\theta}, \ddot{\theta}, \mathbf{X}^{(\cdot)}\right)$ becomes:

$$\tau = \mathbf{f}\left(\theta, \dot{\theta}, \ddot{\theta}, \mathbf{X}^{(\mathbf{B}_0)}\left(\chi^{(\mathbf{p})}\right)\right) \qquad (19)$$

Evaluating equation (19) at multiple trajectory points and adding the nonlinear friction model, we get:

$$\mathbf{Y} = F\left(\theta, \dot{\theta}, \ddot{\theta}, \mathbf{X}^{(\mathbf{B}_0)}\left(\chi^{(\mathbf{p})}\right)\right) + \mathbf{Y}_\mathbf{f}\left(\dot{\theta}, \chi^{(f)}\right) + \rho \qquad (20)$$

Equation (20), expressed in physical parameters, is nonlinear in its parameters and can only be solved by optimization such that it optimizes the values of $\left(\chi^{(\mathbf{p})}\right), \left(\chi^{(\mathbf{f})}\right)$ while minimizing the cost function:

$$\hat{\chi}^{(\mathbf{p},\mathbf{f}),} = \underset{\chi^{(\mathbf{p})}, \chi^{(\mathbf{f})}}{\operatorname{argmin}} \left\| \mathbf{Y} - F\left(\mathbf{X}^{(\mathbf{B}_0)}\left(\chi^{(\mathbf{p})}\right)\right) + \mathbf{Y}_\mathbf{f}\left(\dot{\theta}, \chi^{(f)}\right) \right\|^2 \qquad (21)$$

For the solution of equation (21) to result in physically feasible parameters, some constraints are needed, including linear constraints for masses of links and nonlinear constraints for the inertia tensor $\mathbf{I}_{Gi}$. These constraints can be generally expressed as:

$$\begin{aligned} & m_i > 0 \forall i \\ & \mathbf{I}_{Gi} \text{ is positive definite} \\ & \chi_{lb} \leq \chi \leq \chi_{ub} \end{aligned} \qquad (22)$$

The friction parameters in equation (21) result in a complete dynamic of the modeled system, improving the model's accuracy.

Payload Estimation

The payload may change with robotic applications such as painting and welding. This change impacts the dynamic parameters of the link to which the load is added [40], typically the last link (7th link in this case).

The dynamic parameters of the last link consist of mass $\chi_7^{(m)}$, center of mass, $\chi_7^{(c)} = \left[\chi_{7,x}^{(c)}, \chi_{7,y}^{(c)}, \chi_{7,z}^{(c)}\right]$, and the inertia tensor concerning the link frame:

$$7, \mathbf{X}_7^{(J)} = \left[\mathbf{X}_{7xx}^{(\mathrm{J})}, \mathbf{X}_{7xy}^{(J)}, \mathbf{X}_{7xz}^{(J)}, \mathbf{X}_{7yy}^{(\mathrm{J})}, \mathbf{X}_{7yz}^{(J)}, \mathbf{X}_{7zz}^{(J)}\right].$$

The payload dynamic parameters include mass $\chi_{pl}^{(m)}$, center of mass $\chi_{pl}^{(c)} = \left[\chi_{pl,x}^{(c),}, \left[\chi_{pl,y}^{(c),}, \left[\chi_{pl,z}^{(c),}\right]\right.\right.$, and inertia tensor concerning the link frame $7, \mathbf{X}_{pl}^{(J)}$.

Since the parameters are expressed in the link frame (inertial parameters), linear parametrization is preserved for kinematic conventions.

The new dynamic parameters of the last link (after adding payload) were calculated as follows:

$$\text{Mass: } \chi_7^{(m)} \mapsto \chi_7^{(m)} + \chi_{pl}^{(m)}$$

$$\text{First moment: } \chi_{7,i}^{(c)}\chi_7^{(m)} \mapsto \frac{\chi_{7,i}^{(c)}\chi_7^{(m)} + \chi_{pl,i}^{(c)}\chi_{pl}^{(m)}}{\chi_7^{(m)} + \chi_{pl}^{(m)}}\left(\chi_7^{(m)} + \chi_{pl}^{(m)}\right)$$

$$= \chi_{7,i}^{(c)}\chi_7^{(m)} + \chi_{pl,i}^{(c)}\chi_{pl}^{(m)} \qquad (22)$$

$$\text{Inertia tensor: } \mathrm{X}_7^{(J)} \mapsto \mathrm{X}_7^{(J)} + \mathrm{X}_{pl}^{(J)}$$

$$\text{where } i = x, y, z.$$

The hand of the PANDA robot was used as a payload, which is attached to link 7. The change in dynamic parameters associated with link 7 was due to the payload, as shown in the relationship in equation (22).

Controller Selection

An inverse dynamics controller (Computed Torque Control) was utilized to compute the desired torque from the reference trajectory. Since no external forces were acting on the end effector, we recalled equation (5) and substituted the joint accelerations, $\ddot{\theta}$ with a new term, a_θ. The equation (5) becomes:

$$\tau = M(\theta)a_\theta + c(\theta, \dot{\theta})\dot{\theta} + g(\theta) \qquad (23)$$

Since the inertia matrix $M(\theta)$ is invertible, equations (5) and (23) can be equated, giving a double integrator system:

$$\ddot{\theta} = a_\theta \qquad (24)$$

The equation (24) is linear and decoupled. Assuming that a_θ is a function of joint positions θ and velocities $\dot{\theta}$, then the closed-loop system is decoupled [41]. a_θ was designed to control a second-order linear system by setting:

$$a_\theta = \ddot{\theta}_d - k_d(\dot{\theta} - \dot{\theta}_d) - k_p(\theta - \theta_d) \qquad (25)$$

Equation (25) is a PD control with feed-forward acceleration. Substituting (25) into equation (24), we get:

$$\ddot{\mathrm{e}} + k_d\dot{\mathbf{e}} + k_p\mathbf{e} = 0 \qquad (26)$$

where the error $\mathbf{e} = \theta - \theta_d, \dot{\mathbf{e}} = \dot{\theta} - \dot{\theta}_d, \ddot{\mathbf{e}} = \ddot{\theta} - \ddot{\theta}_d, \ddot{\theta} = a_\theta$ The gain matrices K_p and K_d were chosen as:

$$K_p = \begin{bmatrix} \omega_1^2 & 0 & \cdots & 0 \\ 0 & \omega_2^2 & \cdots & 0 \\ \vdots & & \ddots & \vdots \\ 0 & 0 & \cdots & \omega_n^2 \end{bmatrix}, K_d = \begin{bmatrix} 2\omega_1 & 0 & \cdots & 0 \\ 0 & 2\omega_2 & \cdots & 0 \\ \vdots & & \ddots & \vdots \\ 0 & 0 & \cdots & 2\omega_n \end{bmatrix} \qquad (27)$$

where ω_i for $i \in \{1,7\}$, The natural frequencies determine the rate of decay of the tracking error (the joint's response speed).

Desired Torque

The desired torque, τ_d, was determined from the modified inverse dynamics equation (21).

$$\tau_d = \bar{M}(\theta)a_\theta + \bar{c}(\theta, \dot{\theta})\dot{\theta} + \bar{g}(\theta) \qquad (28)$$

where the inertia matrix $\bar{M}(\theta)$, Coriolis forces $\bar{c}(\theta, \dot{\theta})\dot{\theta}$, and gravity forces vector $\bar{g}(\theta)$ were determined from the Franka Control Interface (FCI controller).

The control input a_θ was then computed using equation (25) with ω_i (PD gain values) given in equation (27), as illustrated in Figure 2.

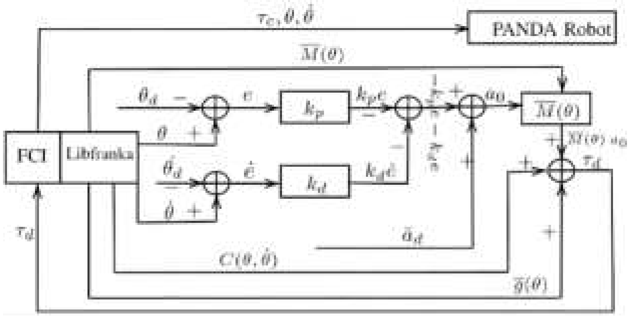

Figure 2: Inverse Dynamics Closed Loop Control employed to track the reference trajectory during identification.

Experimental Setup and Data Acquisition

Real-time commands were transmitted via User Datagram Protocol (UDP) at a frequency of 1 kHz using the Franka Control Interface (FCI). The user sends desired joint positions (θ_d), velocities ($\dot{\theta}_d$), and torques (τ_d) to the FCI, which then calculates the required control torques (τ_c) and sends them to the robot. The robot's encoders return the actual joint positions, velocities, and torques to the FCI. Using this feedback, the FCI computes essential components, such as the mass matrix $\bar{M}(\theta)$, the Coriolis matrix $\bar{C}(\theta, \dot{\theta})$, and the gravity vector $\bar{g}(\theta)$. These values are the real measurements of the robot's state.

All recorded measurements were subject to noise. This was filtered using Matlab's low-pass 'movmean' function, which effectively smooths out high-frequency noise by calculating the local mean of the data within a specified sliding window while preserving the overall data trend. The plotting for the raw and the filtered measurements are represented in plots for joints 1-7 in Figure A1 (a-g) in the Appendix 1. The filtering effectively reduced the noise in the measured signal in all joints, as indicated by visual inspection.

Identification Method

The dynamic parameters, $\hat{\chi}^{(\mathbf{p})}$, were estimated using equation (21) with Lasso regularisation. The fmincon solver from Matlab was used where the optimization problem is represented as:

$$\hat{\chi} = \underset{\chi^{(\mathbf{p})},\chi^{(\mathbf{f})}}{\operatorname{argmin}} \Sigma \left(Y - F\left(\mathbf{X}^{(\mathbf{B_0})}\left(\chi^{(\mathbf{p})}\right)\right) + \mathbf{Y_f}\left(\dot{\theta},\chi^{(f)}\right)\right)^2 + \lambda\Sigma\left|\left(\chi^{(\mathbf{p})},\chi^{(\mathbf{f})}\right)\right| \quad (29)$$

RESULTS AND DISCUSSION

This section presents the estimated physical parameters, friction parameters, and payload results. The robot was controlled using an inverse dynamics controller to track the desired trajectory, facilitating parameter excitation. Torque measurements and *robot* states, acquired via the Franka Control Interface, were utilized for parameter estimation as outlined in the sub-subsection.

1.1.

Experimental Setup and Data Acquisition.

Firstly, the physical parameters were estimated without a friction model using equation (30) to assess the importance of friction torques.

$$\hat{\chi}^{(\mathbf{p})} = argmin \left\| (Actuator + Grav) - F\left(\mathbf{X}^{(\mathbf{B_0})}\left(\chi^{(\mathbf{p})}\right)\right)\right\| + \lambda\Sigma\left|\left(\chi^{(\mathbf{p})}\right)\right| \quad (30)$$

Upon comparing the estimated inverse dynamics torques (using retrieved parameters) with the measured torques, discrepancies were observed, particularly in joints 5, 6, and 7, and mainly attributed to unmodelled friction torques. Friction models were added to the inverse dynamics model to address these discrepancies, as described in the subsection Friction Models.

$$\hat{\chi}^{(\mathbf{p,f})} = \underset{\chi^{(\mathbf{p})},\chi^{(\mathbf{f})}}{\operatorname{argmin}} \left\| \tau_{\text{meas}} - F\left(\mathbf{X}^{(\mathbf{B_0})}\left(\chi^{(\mathbf{p})}\right)\right) + \mathbf{Y_f}\left(\dot{\theta},\chi^{(f)}\right)\right\|^2 + \lambda\Sigma\left|\left(\chi^{(\mathbf{p})},\chi^{(\mathbf{f})}\right)\right| \quad (31)$$

For each added friction model, the physical and friction parameters relevant to that model were retrieved (equation (31)). This approach effectively minimized the difference between the measured and the new estimated torques.

Estimated Physical and Friction Parameters Based on the Lugre, Stribeck, and Sigmoidal Friction Models

The estimated physical parameters with the Lugre Friction model and the Lugre Friction parameters are presented in Tables 2(a) and 2(b), respectively, in Appendix 2. The estimated physical parameters with the Stribeck Friction model and the Stribeck Friction parameters are presented in Tables 3(a) and 3(b). In comparison, the estimated physical parameters with the Sigmoidal Friction model and the Sigmoidal Friction parameters are presented in Tables 4(a) and 4(b), respectively, all in Appendix 2.

The estimated physical parameters resulted in positive masses and positive definite inertia tensors with positive diagonal elements $\left(I_{xx}, I_{yy}, I_{zz}\right)$ in the center of mass (COM) frame. These positive values are essential for the feasibility of the physical parameters. The off-diagonal elements of the inertia tensor $\left(I_{xy}, I_{xz}, I_{yz}\right)$ are typically small and can have any sign. These off-diagonal elements may sometimes be neglected and driven to zero by regularization.

To effectively display the results and evaluate discrepancies, we generated plots for each joint, comparing estimated joint torques over time using the inverse dynamics model combined with specific friction models, as shown in Figures 3(a-g). These included the no-friction and Lugre, Stribeck, and Sigmoidal friction models. By visually comparing the performance of these combined models, we aimed to assess their performance in Figure 3.

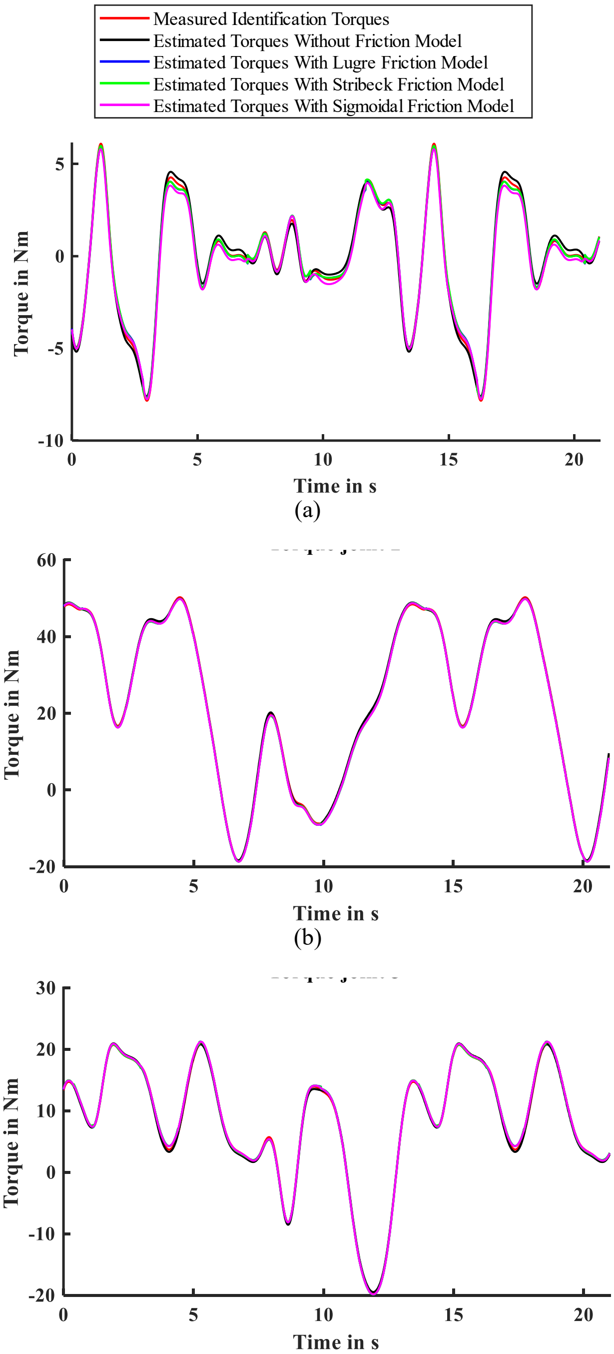

(a)

(b)

(c)

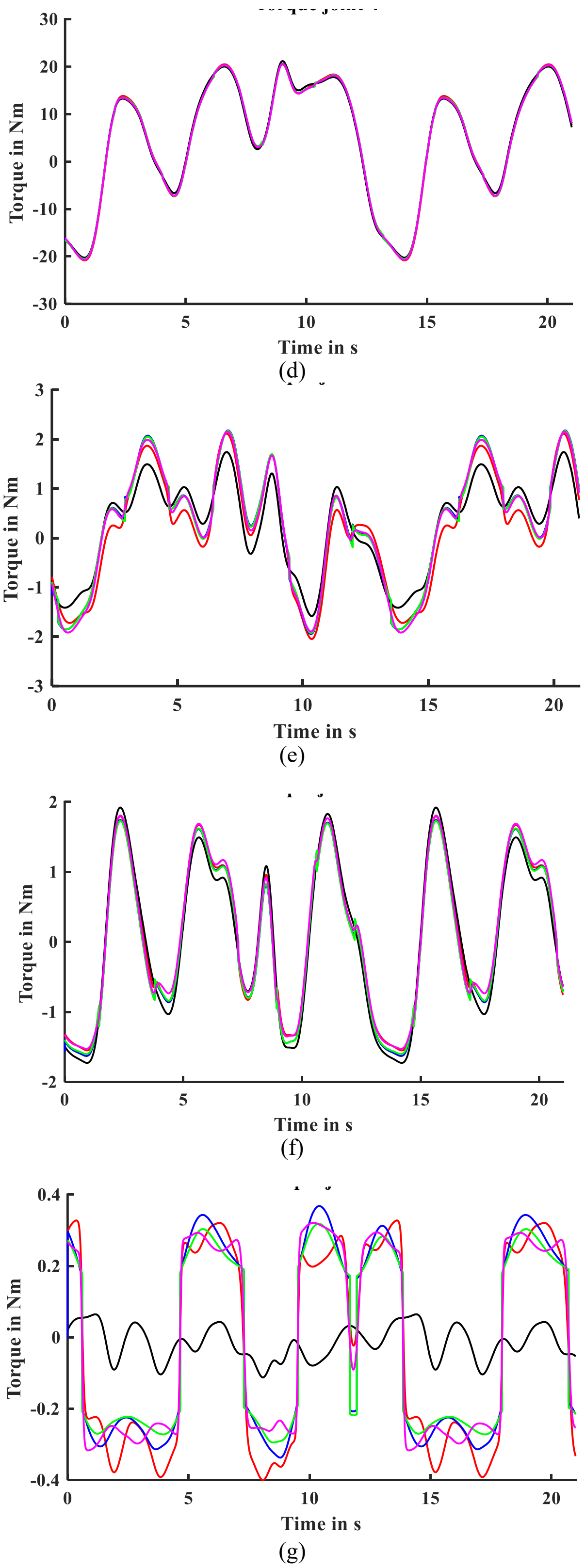

(d)

(e)

(f)

(g)

Figure 3(a-g): Plots of Measured Identification joint torques, Approximated Identification joint torques without friction model for joints 1-7.

A comparison of the plots shows that torque estimates without a friction model have more significant discrepancies when compared to measured torques, especially in joints 5 to 7. However, these discrepancies are significantly reduced when friction models are incorporated.

Payload (Hand) Estimation

The hand of the PANDA robot was used as a fixed payload, as it is attached to the last link, and the new inertial parameters of link 7 were formulated using equation 20. An experiment was conducted with the robot's hand attached, employing the identification trajectory, and the joint torques, positions, and velocities were measured. Using these measurements, the physical parameters of link 7 were estimated, as shown in Table 5.

Table 5: The estimated physical parameters for link 7 with the robot's Hand attached as a payload.

Variable	Ixx	Iyy	Izz	Ixy	Ixz
Units	$kg.m^2$	$kg.m^2$	$kg.m^2$	$kg.m^2$	$kg.m^2$
Value	0.0167	0.0001	0.0034	-0.0006	0.0003
Variable	Iyz	rx	ry	rz	Mass
Units	$kg.m^2$	m	m	m	kg
Value	0.0004	-0.0067	0.0062	0.0485	1.6093

The formula approximated the hand of the robot:

$$\text{Mass}_{\text{Payload}} \approx \text{Mass}_{\text{link 7(WithHand)}} - \text{Mass}_{\text{link 7(WithoutHand)}}$$
$$\approx 1.6093 - 0.5416$$
$$\approx 1.0677\ kg$$

Validation

Before applying the model, a validation process was crucial to prevent undesired or hazardous outcomes. As such, the model validation phase was employed to establish the reliability of the estimated parameters and determine the model's suitability for practical applications such as control or simulation.

The Newton-Euler (NE) inverse dynamics model was employed to validate the estimated parameters, incorporating the estimated inertial parameters obtained from the physical and friction parameters to calculate the torques. Validation torque measurements were obtained by running a distinct validation trajectory separate from the identification trajectory. This was plotted, and a visual comparison was conducted between the measured and approximated torques in Figures 4(a-g).

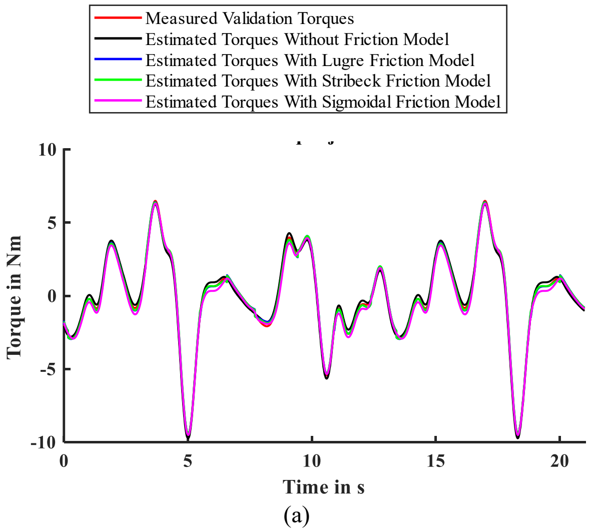

(a)

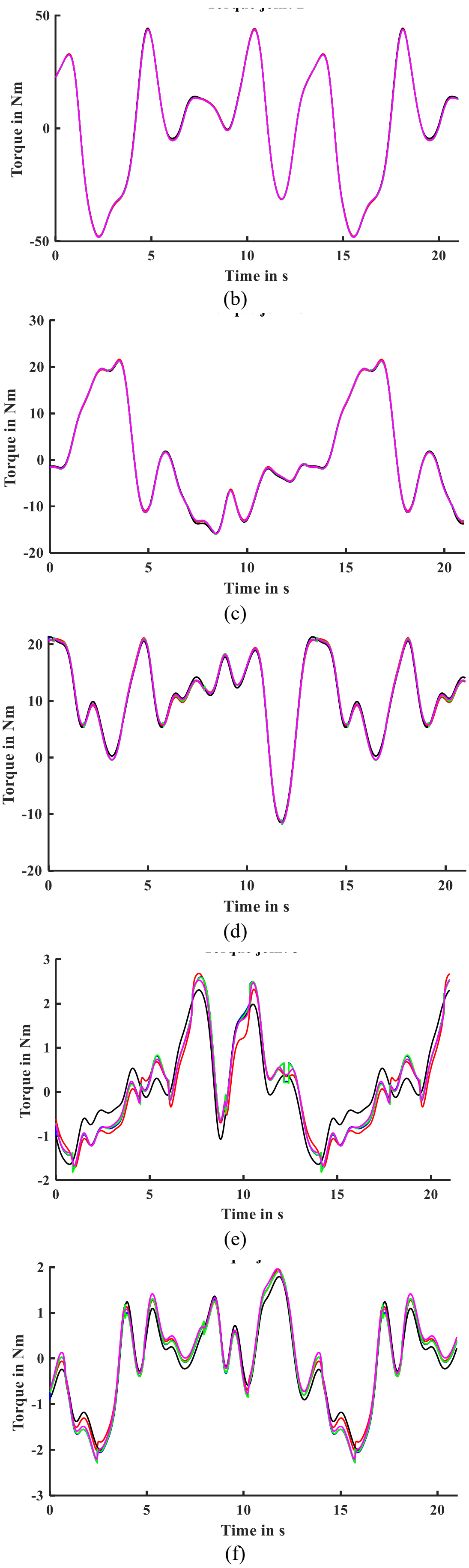

(b)

(c)

(d)

(e)

(f)

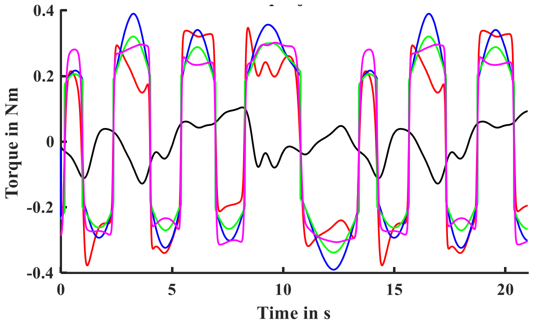

(g)

Figure 4(a-g): Plots of Measured Validation joint torques, Approximated Validation joint torques without friction model for joints 1-7.

From the validation plots, we observed that the estimated parameters incorporating friction models provided a reasonable estimate of validation torques, as the discrepancy between calculated and measured torques (the prediction error) was minimal. This result indicated that the estimated parameters were not over-fitted to the training data. The model joints with less accurate parameter estimates were identified by visualizing the prediction error. To gain further insight into the model's quality and the performance of individual joints, the root means square error (RMSE) and mean absolute error (MAE) of the prediction errors were calculated.

Comparing Root Mean Square Error (RMSE) and Mean Absolute Error (MAE) Values for Model Evaluation

The Root Mean Square Errors (RMSE) were calculated (Appendix 2 Table 6 (a) and (b)) to determine the standard deviation of residuals (how far data points are from the regression line) using the equation:

$$RMSE = \sqrt{\frac{\sum_{i=1}^{N} (\text{ Estimated }_i - \text{ Measured }_i)^2}{N}} \tag{32}$$

Where N is the number of data points:

Generally, a lower RMSE value indicates a better approximation. In the identification phase, the Stribeck friction model shows the best overall performance, with a mean RMSE of 0.1904, outperforming the Lugre (0.1920) and Sigmoidal (0.1955). The model without friction performs the worst, particularly in joint 4, which records the highest RMSE (0.5325). The Sigmoidal model performs better in joints with lower torques, especially in joint 6 (0.0583) with the lowest identification RMSE.

For validation, the Stribeck model also provides the best results with a mean RMSE of 0.1855, followed by Lugre (0.1894) and Sigmoidal (0.1939). Joint 6 again shows the lowest RMSE (0.0993) using the Sigmoidal model. The model without friction consistently performs poorly in the identification and validation phases.

Overall, the Stribeck model offers the best balance between accuracy in identification and validation, though the Sigmoidal model is superior in scenarios involving lower joint torques.
Since RMSE penalizes more significant errors aggressively than MAE, it is more sensitive to critical errors. To avoid this potential problem, MAE values were also computed for verification since

they handle all errors uniformly and provide a fairer assessment of general prediction accuracy. MAE values were formulated using the equation:

$$MAE = \frac{\sum_{i=1}^{N} \mid \text{Estimated}_{\,i} - \text{Measured}_{\,i} \mid}{N}$$

Table 7 (a) and (b) (in Appendix 2) presents the MAE Values for the Identification and Validation of Torques with Different Friction Models. Just like in RMSE, a lower MAE value indicates a better approximation.

In the identification phase, the model with Stribeck friction offers the best performance with a mean MAE of 0.1532, outperforming the Lugre friction model (0.1554) and the Sigmoidal friction model (0.1597). The model without friction performs the worst, with a mean MAE of 0.3151. Joint 4 has the highest identification MAE without friction (0.4986). On the other hand, the Sigmoidal friction model performs better in joints with lower torques, as shown by its lowest MAE in joint 6 (0.0445).

For validation, the Stribeck friction model again achieves the lowest mean MAE of 0.1535, showing a consistent edge over the Lugre friction model (0.1553) and the Sigmoidal friction model (0.1640). The model without friction continues to perform poorly, with the highest mean MAE (0.3160) and the highest individual validation MAE for joint 4 (0.5509). Like the identification phase, the Sigmoidal friction model delivers the lowest validation MAE in joint 6 (0.0836).

The Stribeck friction model consistently demonstrates the best overall performance in RMSE and MAE across the identification and validation phases. Specifically, the Stribeck model achieves the lowest mean RMSE and MAE values, followed closely by the Lugre model and then the Sigmoidal model. Notably, the Sigmoidal model excels in scenarios involving lower torques, such as in joints 5 and 6. However, it does not surpass the Stribeck model in overall accuracy.

The model without friction consistently performs the worst in both metrics, highlighting the importance of including friction models. The RMSE and MAE values confirm that including a friction model results in lower RMSE and MAE values for identification and validation torques. Therefore, we analytically confirm that incorporating friction models when estimating parameters provides more accurate joint torque approximations than estimates without friction models.

CONCLUSION

In conclusion, this study has demonstrated the linear and nonlinear parameter identification models and investigated nonlinear friction models, specifically for the PANDA robot manipulator. The results indicate that the identification model with Stribeck friction incorporated provided the best parameter approximation, followed by the Lugre and Sigmoidal friction models. Friction torques were found to play a significant role in joints 5, 6, and 7, where the torques are below 2.5Nm and cannot be neglected. The analysis further revealed that the joint flexibility and rotor inertia, which were not modeled in this study, did not considerably impact the identification model for the PANDA robot manipulator. This work provides valuable insights into the dynamic parameter identification of robot manipulators and can serve as a foundation for future research in this area.

As a continuation of the findings of this research, future work could focus on extending the parameter identification methods to address time-varying payloads and friction parameters of the same robot through an online identification process. Additionally, incorporating rotor inertia and joint flexibility models may enhance the model's accuracy. The implementation of adaptive control strategies could be investigated to improve the robot's performance in the presence of uncertainties and disturbances. Finally, evaluating the proposed methodologies on other robot manipulator models with varying degrees of complexity and different friction characteristics would contribute to the generalizability of the findings and promote a broader understanding of dynamic parameter identification in robot manipulators.

ACKNOWLEDGEMENT

The experimental research was made possible through the facilities and support provided by the Department of Electrical and Computer Engineering at the Technical University of Kaiserslautern. The authors are deeply grateful for the invaluable assistance and resources available during this study.

REFERENCES

[1] H. Choi, C. Crump, C. Duriez, A. Elmquist, G. Hager, D. Han, F. Hearl, J. Hodgins, A. Jain, F. Leve *et al.*, “On the use of simulation in robotics: Opportunities, challenges, and suggestions for moving forward,” *Proceedings of the National Academy of Sciences*, vol. 118, no. 1, p. e1907856118, 2021.

[2] L. Zlajpah, “Simulation in robotics,” *Mathematics and Computers in Simulation*, vol. 79, no. 4, pp. 879–897, 2008, 5th Vienna International Conference on Mathematical Modelling/Workshop on Scientific Computing in Electronic Engineering of the 2006 International Conference on Computational Science/Structural Dynamical Systems: Computational Aspects. [Online]. Available: https://www.sciencedirect. com/science/article/pii/S0378475408001183

[3] Z. Wang, Y. Sun, B. Cao, and G. Liu, “Model predictive control of robot manipulators: A review,” *IEEE Access*, vol. 6, pp. 13945–13963, 2018.

[4] M. Schwenzer, M. Ay, T. Bergs, and D. Abel, “Review on model predictive control: An engineering perspective,” *The International Journal of Advanced Manufacturing Technology*, vol. 117, no. 5-6, pp. 1327–1349, 2021.

[5] K. Holkar and L. M. Waghmare, “An overview of model predictive control,” *International Journal of control and automation*, vol. 3, no. 4, pp. 47–63, 2010.

[6] A. Kazemipour, O. Fischer, Y. Toshimitsu, K. W. Wong, and R. K. Katzschmann, “Adaptive dynamic sliding mode control of soft continuum manipulators,” in *2022 International Conference on Robotics and Automation (ICRA)*. IEEE, 2022, pp. 3259–3265.

[7] V. Azizi, A. Shahrooei, and N. Sadati, “Modeling and control of collaborative robots,” *IEEE Transactions on Systems, Man, and Cybernetics: Systems*, 2019.

[8] T. George Thuruthel, F. Renda, and F. Iida, “First-order dynamic modeling and control of soft robots,” *Frontiers in Robotics and AI*, vol. 7, p. 95, 2020.

[9] W. Zhang, M. Tognon, L. Ott, R. Siegwart, and J. Nieto, "Active model learning using informative trajectories for improved closed-loop control on real robots," in *2021 IEEE International Conference on Robotics and Automation (ICRA)*. IEEE, 2021, pp. 4467–4473.

[10] F. Sherwani, M. M. Asad, and B. S. K. K. Ibrahim, "Collaborative robots and industrial revolution 4.0 (ir 4.0)," in *2020 International Conference on Emerging Trends in Smart Technologies (ICETST)*. IEEE, 2020, pp. 1–5.

[11] A. Hassani, A. Bataleblu, S. Khalilpour, H. D. Taghirad, and P. Cardou, "Dynamic models of spherical parallel robots for model-based control schemes," *arXiv preprint arXiv:2110.00491*, 2021.

[12] M. E. A. Boudella, E. Sahin, and Y. Dallery, "Kitting optimisation in just-in-time mixed-model assembly lines: assigning parts to pickers in a hybrid robot–operator kitting system," *International Journal of Production Research*, vol. 56, no. 16, pp. 5475–5494, 2018.

[13] M. Javaid, A. Haleem, R. P. Singh, and R. Suman, "Substantial capabilities of robotics in enhancing industry 4.0 implementation," *Cognitive Robotics*, vol. 1, pp. 58–75, 2021.

[14] J. Fisel, Y. Exner, N. Stricker, and G. Lanza, "Changeability and flexibility of assembly line balancing as a multi-objective optimization problem," *Journal of manufacturing systems*, vol. 53, pp. 150–158, 2019.

[15] L. Manfredi, A. Censi, L. Fadiga, G. Gini, E. Guglielmelli, C. Laschi, H. Marino, P. Morasso, L. Natale, A. Oddera *et al.*, "From human to robot sensorimotor coordination," *Frontiers in neurorobotics*, vol. 12, 2018.

[16] T. Ji, A. N. Sivakumar, G. Chowdhary, and K. Driggs-Campbell, "Proactive anomaly detection for robot navigation with multi-sensor fusion," *IEEE Robotics and Automation Letters*, vol. 7, no. 2, pp. 4975–4982, 2022.

[17] V. Lyashenko and S. Sotnik, "Analysis of basic principles for sensor system design process mobile robots," *Journal La Multiapp*, vol. 1, no. 4, pp. 1–6, 2020.

[18] X. Wu, F. Gao, S. S. Ge, and H. Ren, "A survey on optimal control of robotic manipulators: Methods, applications, and perspectives," *IEEE Access*, vol. 7, pp. 123003–123019, 2019.

[19] S. Danthala, S. Rao, K. Mannepalli, and D. Shilpa, "Robotic manipulator control by using machine learning algorithms: A review," *International Journal of Mechanical and Production Engineering Research and Development*, vol. 8, no. 5, pp. 305–310, 2018.

[20] P. Mesmer, M. Neubauer, A. Lechler, and A. Verl, "Robust design of independent joint control of industrial robots with secondary encoders," *Robotics and Computer-Integrated Manufacturing*, vol. 73, p. 102232, 2022.

[21] W. Khalil and E. Dombre, "Dynamic modeling and identification," *Springer Tracts in Advanced Robotics*, vol. 130, pp. 29–66, 2017.

[22] M. R. Kermani, R. V. Patel, and M. Moallem, "Friction identification and compensation in robotic manipulators," *IEEE Transactions on Instrumentation and Measurement*, vol. 56, no. 6, pp. 2346–2353, 2007.

[23] J. Wu, J. Wang, and Z. You, "An overview of dynamic parameter identification of robots," *Robotics and computer-integrated manufacturing*, vol. 26, no. 5, pp. 414–419, 2010.

[24] A. Tika, J. Ulmen, and N. Bajcinca, "Dynamic parameter estimation utilizing optimized trajectories," in *2020 IEEE/RSJ International Conference on Intelligent Robots and Systems (IROS)*. IEEE, 2020, pp. 7300–7307.

[25] C. Gaz, M. Cognetti, A. Oliva, P. R. Giordano, and A. De Luca, "Dynamic identification of the franka emika panda robot with retrieval of feasible parameters using penalty-based optimization," *IEEE Robotics and Automation Letters*, vol. 4, no. 4, pp. 4147–4154, 2019.

[26] Y. R. Sturz, L. M. Affolter, and R. S. Smith, "Parameter identification¨ of the kuka lbr iiwa robot including constraints on physical feasibility," *IFAC-PapersOnLine*, vol. 50, no. 1, pp. 6863–6868, 2017.

[27] L. Ding, X. Li, Q. Li, and Y. Chao, "Nonlinear friction and dynamical identification for a robot manipulator with improved cuckoo search algorithm," *Journal of Robotics*, vol. 2018, pp. 1–10, 2018.

[28] C. Gaz, F. Flacco, and A. De Luca, "Identifying the dynamic model used by the kuka lwr: A reverse engineering approach," in *2014 IEEE international conference on robotics and automation (ICRA)*. IEEE, 2014, pp. 1386–1392.

[29] A. Awatef and B. H. Mouna, "Dynamic modeling and inverse dynamic control of mobile robot," in *2017 International Conference on Green Energy Conversion Systems (GECS)*. Ieee, 2017, pp. 1–5.

[30] C. Gaz, F. Flacco, and A. De Luca, "Extracting feasible robot parameters from dynamic coefficients using nonlinear optimization methods," in *2016 IEEE international conference on robotics and automation (ICRA)*. IEEE, 2016, pp. 2075–2081.

[31] A. Jubien, M. Gautier, and A. Janot, "Dynamic identification of the kuka lwr robot using motor torques and joint torque sensors data," *IFAC Proceedings Volumes*, vol. 47, no. 3, pp. 8391–8396, 2014.

[32] E. Magrini and A. De Luca, "Hybrid force/velocity control for physical human-robot collaboration tasks," in *2016 IEEE/RSJ International Conference on Intelligent Robots and Systems (IROS)*. IEEE, 2016, pp. 857–863.

[33] C. D. Sousa and R. Cortesao, "Inertia tensor properties in robot dynamics identification: A linear matrix inequality approach," *IEEE/ASME Transactions on Mechatronics*, vol. 24, no. 1, pp. 406–411, 2019.

[34] W. Khalil and J. Kleinfinger, "A new geometric notation for open and closed-loop robots," in *Proceedings. 1986 IEEE International Conference on Robotics and Automation*, vol. 3. IEEE, 1986, pp. 1174–1179.

[35] W. Khalil, A. Vijayalingam, B. Khomutenko, I. Mukhanov, P. Lemoine, and G. Ecorchard, "Opensymoro: An open-source software package for symbolic modelling of robots," in *2014 IEEE/ASME International Conference on Advanced Intelligent Mechatronics*. IEEE, 2014, pp. 1206–1211.

[36] Z. Shareef, P. Mohammadi, and J. Steil, "Improving the inverse dynamics model of the kuka lwr iv+ using independent joint learning," *IFACPapersOnLine*, vol. 49, no. 21, pp. 507–512, 2016.

[37] C. Frank, *Modern Robotics-Mechanics, Planning, and Control*. Cambridge University Press, 2017.

[38] M. Gautier and W. Khalil, "On the identification of the inertial parameters of robots," in *Proceedings of the 27th IEEE Conference on Decision and Control*, vol. 3. IEEE Austin, 1988, pp. 2264–2269.

[39] C. D. Sousa and R. Cortesao, "Physical feasibility of robot base inertial parameter identification: A linear matrix inequality approach," *The International Journal of Robotics Research*, vol. 33, no. 6, pp. 931–944, 2014.

[40] A. De Luca, "Linear parametrization and identification of robot dynamics."

[41] M. W. Spong, S. Hutchinson, and M. Vidyasagar, *Robot modelling and control*. John Wiley & Sons, 2020.

[42] A. Rogel, R. Savery, N. Yang, and G. Weinberg, 'RoboGroove: Creating Fluid Motion for Dancing Robotic Arms', in *Proceedings of the 8th International Conference on Movement and Computing*, Chicago, IL, USA, 2022.

Appendix 1

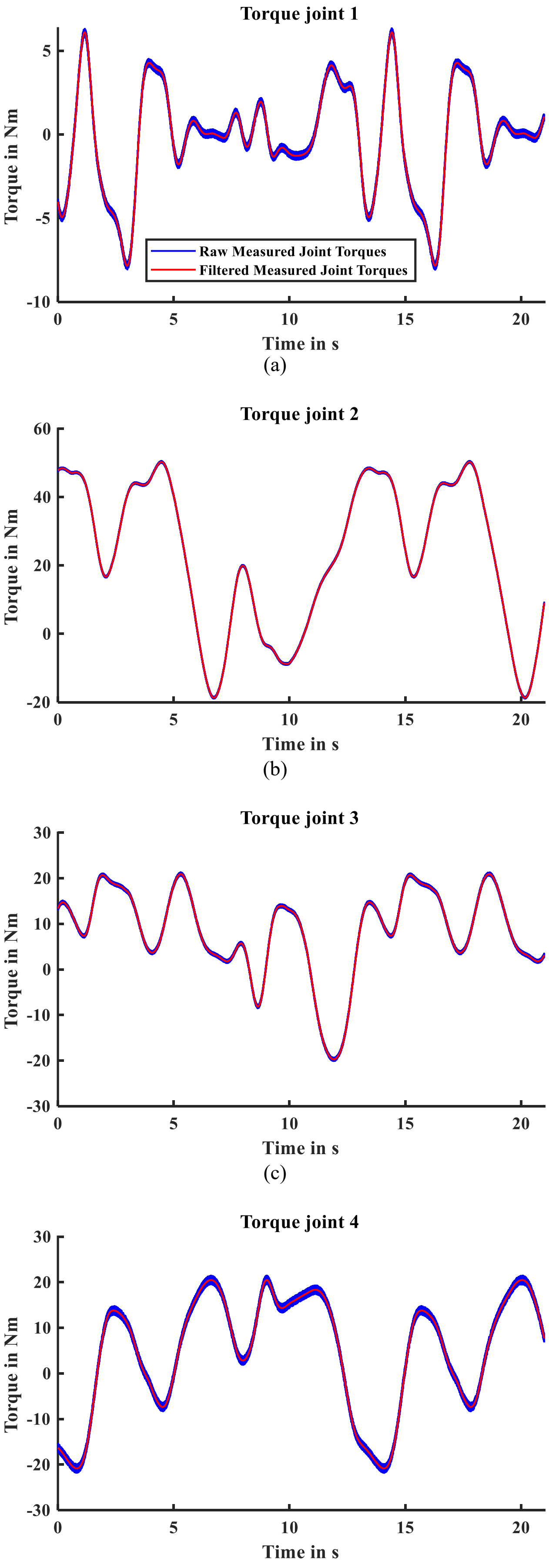

(a)

(b)

(c)

(d)

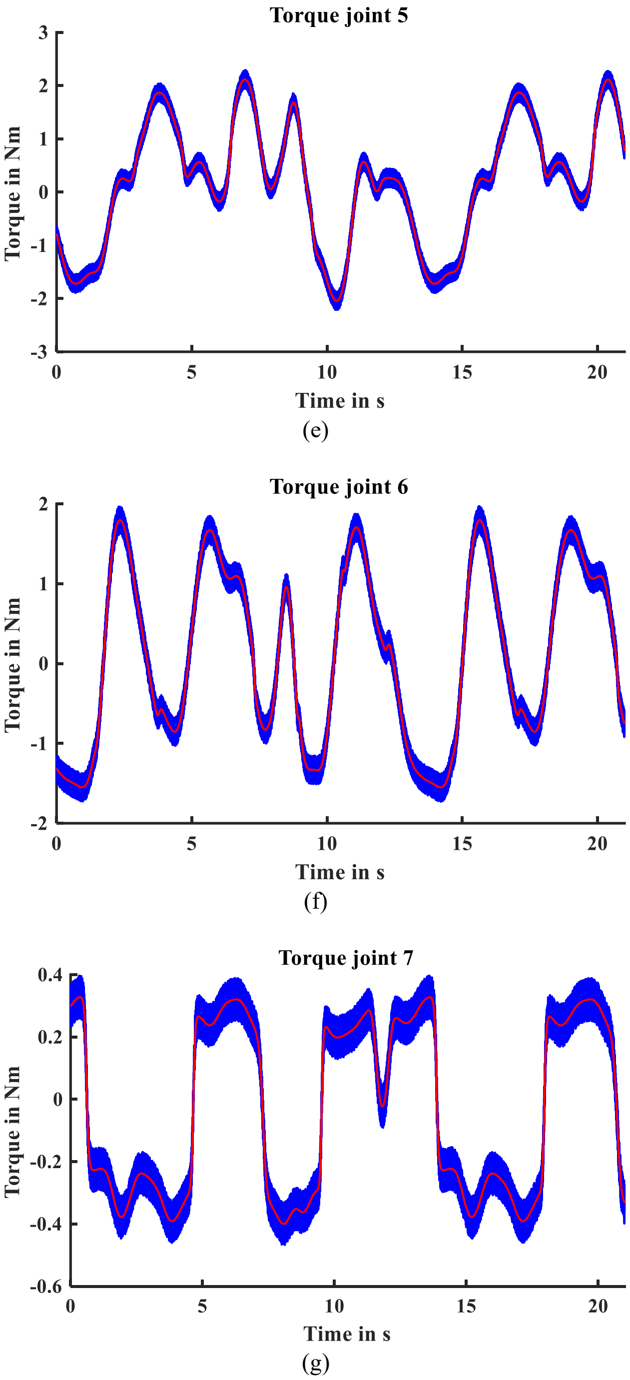

(e)

(f)

(g)

Figure A1 (a-g): Plots of raw Measured Identification torques (Blue) joints (1-7) and filtered Measured Identification torques (Red

Appendix 2

Table 2(a): Estimated Physical Parameters with Lugre Friction Model

	Link 1	Link 2	Link 3	Link 4	Link 5	Link 6	Link 7
Ixx (kg·m²)	0.5	0.0752	0.0528	0.0285	0.0669	0.0066	0.0005
Iyy (kg·m²)	0.5	0.0297	0.0102	0.0064	0.0534	0.0053	0.0019
Izz (kg·m²)	0	0.016	0.0183	0.0486	0.0022	0.0006	0.0001
Ixy (kg·m²)	7.72E-14	0.0098	-0.0195	0.0072	-0.0039	-0.0033	-0.0009
Ixz (kg·m²)	-8.56E-10	-0.02	-0.0298	-0.0241	-0.0112	-0.0002	-0.0002
Iyz (kg·m²)	8.55E-10	-0.0201	0.0131	0.0053	0.0048	0.0015	0.0005
rx (m)	-3.48E-08	0.0396	0.0345	-0.0474	-0.0016	0.0733	-0.0015
ry (m)	-3.48E-08	-0.1222	0.0351	0.1385	0.0307	-0.0205	0.004
rz (m)	-0.175	-0.0096	-0.0999	0.0327	-0.125	-0.0262	0.0638
Mass (kg)	4.75	0.9918	3.2832	3.5858	1.3628	1.741	0.5158

Table 2(b): Lugre Friction Parameters

Joints	σ_0 (N·m)	σ_1 (N·m)	σ_2 (N·m)	σ_3 (N·m)	v_0 (rad/s)	v_1 (rad/s)	v_2 (rad/s)
1	0.2390	0.0435	0.0316	0.4999	6.1102e-05	3.9028e-05	4.5659e-04
2	0.1360	0.1356	0.1795	0.4999	6.4280e-05	3.6342e-05	1.6242e-03
3	0.1764	0.0601	0.0663	0.4999	5.3066e-05	1.6280e-05	5.7174e-04
4	0.3662	0.1631	0.1772	0.4999	6.8089e-05	4.4244e-05	1.0923e-04
5	0.2152	0.0616	0.1082	0.5000	7.3521e-05	7.3274e-05	1.7022e-03
6	0.1398	0.0591	0.0192	0.5000	5.8370e-05	5.6923e-05	1.0196e-03
7	0.1837	0.0471	0.0997	0.5000	7.6521e-05	3.8782e-05	2.4456e-03

Tables 2(a) and 2(b) present the estimated physical parameters of the robot and the friction parameters, respectively, based on the Lugre friction model.

Table 3(a): Estimated Physical Parameters with Stribeck Friction Model

	Link 1	Link 2	Link 3	Link 4	Link 5	Link 6	Link 7
Ixx (kg·m²)	0.5	0.108	0.0438	0.0475	0.0394	0.0021	0.0001
Iyy (kg·m²)	0.5	0.0269	0.0031	0.0036	0.0246	0.0024	0.0003
Izz (kg·m²)	1.19E-16	0.0154	0.0255	0.0685	0.0034	0.0005	5.15E-05
Ixy (kg·m²)	8.91E-13	-0.0006	-0.0115	0.0098	-0.0038	-0.0019	-0.0002
Ixz (kg·m²)	-8.97E-10	-0.019	-0.0333	-0.0166	-0.0115	-0.0006	-8.44E-05
Iyz (kg·m²)	8.98E-10	-0.0178	0.0088	0.0066	-0.0004	0.001	0.0001
rx (m)	-6.94E-09	0.0392	0.0381	-0.051	-0.0019	0.0743	-0.0005
ry (m)	-6.94E-09	-0.1485	0.0273	0.146	0.0412	-0.0255	0.0044
rz (m)	-0.175	-0.0154	-0.0968	0.026	-0.1109	-0.0205	0.0478
Mass (kg)	4.75	1.0148	3.3381	3.5646	1.2652	1.6728	0.5416

Table 3(b:) Stribeck Friction Parameters

Joints	F_C(Nm)	F_V(Nm·s/rad)	F_s (Nm)	V_s (m/s)	K_S
1	0.2247	0.0497	6.5038e-22	2.1749	2.1748
2	0.1293	0.1708	-8.6085e-28	2.1749	2.1748
3	0.1681	0.0774	1.6565e-20	2.1749	2.1748
4	0.3791	0.1792	5.8329e-24	2.1749	2.1748
5	0.2231	0.1038	3.7780e-25	1.5208	1.3656
6	0.1497	0.0129	7.4546e-22	1.5207	1.3656
7	0.1936	0.0655	2.7360e-21	1.5207	1.3656

Tables 3(a) and 3(b) present the estimated physical parameters of the robot and the friction parameters, respectively, based on the Stribeck friction model.

Table 4(a): Estimated Physical Parameters with Sigmoidal Friction Model

	Link 1	Link 2	Link 3	Link 4	Link 5	Link 6	Link 7
Ixx (kg·m²)	0.5	0.061	0.0153	0.0605	0.029	0.0043	0.0012
Iyy (kg·m²)	0.5	0.0363	0.0054	0.0103	0.027	0.0012	2.63E-05
Izz (kg·m²)	0	0.0357	0.0085	0.0875	0.005	0.0001	4.01E-05
Ixy (kg·m²)	-1.53E-13	0.0192	-0.0071	0.0089	0.002	-0.002	-0.0002
Ixz (kg·m²)	1.30E-09	-0.0258	-0.0095	-0.0398	-0.0095	-7.31E-05	-0.0002
Iyz (kg·m²)	1.30E-09	-0.0355	0.0067	0.0177	0.0064	0.0002	3.24E-05
rx (m)	-5.14E-09	0.0285	0.0361	-0.049	-0.0034	0.0693	-0.0044
ry (m)	-5.14E-09	-0.1348	0.05	0.1443	0.0415	-0.0255	0.0047
rz (m)	-0.175	-0.05	-0.1	0.048	-0.1317	-0.021	0.04
Mass (kg)	4.75	1.0207	3.3483	3.5444	1.2453	1.6884	0.6385

Table 4(b): Sigmoidal Friction Parameters

Joints	ψ_1 (N·m)	ψ_2 (1/(rad/s))	ψ_3 (rad/s)
1	0.6183	10.8798	0.1120
2	0.5428	10.8708	0.0472
3	0.5048	10.8739	-0.0111
4	0.9740	10.8846	0.0158
5	0.6200	13.0489	0.0053
6	0.3491	13.0484	-0.0765
7	0.5572	13.0473	0.0010

Tables 4(a) and (b) present the estimated physical parameters of the robot and the friction parameters, respectively, based on the Sigmoidal friction model.

Table 6(a): RMSE Values for the Identification of Torques with Different Friction Models

Identification RMSEs				
Joints	Without Friction	With Lugre Friction	With Stribeck Friction	With Sigmoidal Friction
1	0.252	0.1476	0.1348	0.2241
2	0.4121	0.3366	0.3423	0.3606
3	0.2941	0.2514	0.248	0.2389
4	0.5325	0.248	0.25	0.2213
5	0.3865	0.2128	0.2072	0.1914
6	0.1545	0.0739	0.0732	0.0583
7	0.2683	0.0737	0.0773	0.0742
Mean RMSEs	0.3286	0.192	0.1904	0.1955

Table 6(b): RMSE Values for the Validation of Torques with Different Friction Models

Validation RMSEs				
Joints	Without Friction	With Lugre Friction	With Stribeck Friction	With Sigmoidal Friction
1	0.2148	0.1305	0.1249	0.2094
2	0.3946	0.4637	0.472	0.4282
3	0.2996	0.1691	0.1688	0.1582
4	0.5726	0.1947	0.1836	0.2287
5	0.3967	0.1661	0.1625	0.1543
6	0.1549	0.1111	0.1078	0.0993
7	0.266	0.0906	0.0788	0.0792
Mean RMSEs	0.3285	0.1894	0.1855	0.1939

Tables 6(a) and 6(b) show the RMSE values for Identification and validation trajectories Torques, respectively.

Table 7(a): MAEs Values for Identification

Identification MAEs				
Joint	Without Friction	With Lugre Friction	With Stribeck Friction	With Sigmoidal Friction
1	0.2437	0.1188	0.1091	0.1907
2	0.4008	0.2897	0.2917	0.3052
3	0.2771	0.1786	0.1747	0.1677
4	0.4986	0.2028	0.2006	0.1857
5	0.3721	0.1786	0.173	0.1604
6	0.1508	0.0601	0.059	0.0445
7	0.2624	0.0593	0.0639	0.0634
Mean MAEs	0.3151	0.1554	0.1532	0.1597

Table 7(b): MAEs Values for Validation

Validation MAEs				
Joint	Without Friction	With Lugre Friction	With Stribeck Friction	With Sigmoidal Friction
1	0.2031	0.1025	0.0992	0.1702
2	0.3783	0.4003	0.4073	0.3791
3	0.2862	0.1363	0.1354	0.1321
4	0.5509	0.1648	0.1564	0.1895
5	0.3821	0.1309	0.132	0.1238
6	0.151	0.0822	0.0793	0.0836
7	0.2604	0.0703	0.065	0.0697
Mean MAEs	0.316	0.1553	0.1535	0.164

Tables 7(a) and 7(b) show the RMSE values for Identification and validation trajectories, respectively.